Multiple cross-gradient joint inversion for geospectral imaging

Luis A. Gallardo[1]

[1]   Accurate characterization and monitoring of complex subsurface environments require the integration of all the available geophysical, geochemical and geological information. I developed a generalized cross-gradient procedure that seeks multiple geometrically similar images that simplify the integration of cross-property subsurface information. I jointly invert near-surface P-wave, S-wave, DC resistivity and magnetic data sets recorded at a field site and compound an integrated subsurface (geospectral) image based on the multiple property images found. It is shown that, by analogy to applications in satellite imagery, the geospectral image assembles the multiple subsurface parameter values under a common structural framework that facilitates their visualization and analysis. **Citation:** Gallardo, L. A. (2007), Multiple cross-gradient joint inversion for geospectral imaging, *Geophys. Res. Lett.*, *34*, L19301, doi:10.1029/2007GL030409.

1.   Introduction

[2]   The combined analysis or fusion of multiple data from physical, chemical or biological observations on geological targets makes possible the discrimination and classification of subsurface materials and processes. Unfortunately, the individual uncertainties and low resolution of some data may mislead an integrated interpretation process. It is now emerging that this interpretation process can be objectively improved when several data sets bearing a common signature of the underlying geology are jointly inverted.

[3]   Some joint inversion approaches rely on gradient-based relationships [see *Gallardo and Meju*, 2003, 2004; *Haber and Oldenburg*, 1997; *Saunders et al.*, 2005; *Zhang and Morgan*, 1996] such as that founded on the cross-gradient constraint [*Gallardo and Meju*, 2003, 2004]. This approach seeks subsurface images with parallel parameter changes that, without restricting the actual parameter values or the magnitude of their variations, may depict a common geological structure. However, the cross-gradient constraint is defined for pairs of parameters and therefore, it has been limited to the combined analysis of only two physical quantities at a time [*Gallardo and Meju*, 2003, 2004, 2007; *Gallardo et al.*, 2005; *Linde et al.*, 2006; *Tryggvason and Linde*, 2006]. It may be expected that the structural resemblance measured by the cross-gradient function should prevail not only between pairs, but among several collocated parameter images. Moreover, if it is properly incorporated in a multiple parameter joint inversion, it should reduce model uncertainty and enhance the contribution of the individual parameters towards a structurally consistent model.

[4]   In this paper, I give evidence that the direction of subsurface parameter variations provides a natural common structural framework in actual geological materials. To explore this framework, I extend the cross-gradient constraint to multiple parameters, develop an algorithm for the joint inversion of multiple property data sets and apply it to field data. I present the results in an enhanced multi-parameter (geospectral) image that introduces a philosophy for the integral visualization and analysis of complex subsurface materials.

2.   Multiple Parameter Joint Inversion
2.1.   Generalized Cross-Gradient Constraint

[5]   As a starting point, I hypothesize that the subsurface can be integrally described by several properties, which are characteristic for distinctive materials and that each one of these properties can be uncoupled and represented in a parameter image. Conversely, I may also conceptualize an integrated subsurface model as an ensemble of such individual parameters and define a geospectral image as an integrated display of more than two collocated subsurface parameters (see Figure 1). In analogy to multi-spectral images obtained from satellite devices, this display may serve for lithotype discrimination, but it will depend on the actual parameter contrasts, the number of analyzed parameter types and their precision. I posit that, without restricting the magnitude of the natural parameter variations, these limitations can be significantly reduced if all the parameter images follow a geometrical distribution determined by a common geological structure. In this regard, I propose a generalized cross-gradient constraint, which will hold for any n two-dimensional collocated images $(m_1, \ldots, m_n)$ of different types of parameters, given by

$$\text{if } |\nabla m_g(x,z)| \neq 0, \text{ then}$$

$$\tau_g(x,z) = \begin{bmatrix} \nabla m_g(x,z) \times \nabla m_1(x,z) \\ \nabla m_g(x,z) \times \nabla m_2(x,z) \\ \vdots \\ \nabla m_g(x,z) \times \nabla m_n(x,z) \end{bmatrix} = \begin{bmatrix} 0 \\ 0 \\ \vdots \\ 0 \end{bmatrix}. \quad (1)$$

This condition implies that if all the collocated non-null parameter gradients are parallel to one of them (∇m_g), then, they are all parallel to each other. These conditions yield the constraints required to force the geometrical similarity of all the parameter images.

[1]Earth Science Division, Centro de Investigación Científica y Educación Superior de Ensanada, Ensenada, Mexico.
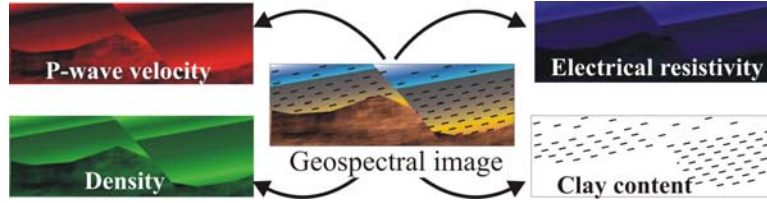
Figure 1. Illustration of a geospectral image and its decoupling into individual images that follow the same underlying structure.

2.2. Numerical Procedure for Multiple Joint Inversion

[6] I can define the multiple cross-gradient 2D joint inversion as the search for n 2D subsurface images (m_1, m_2, …, m_n) that are geometrically similar and satisfy their respective geophysical, geochemical, geological observations within their observation errors. However, as pointed out by *Gallardo et al.* [2005], there can be several image ensembles that equally satisfy these two conditions. I thus add zero and second order Tikhonov regularizations, which are combined in the following objective function:

$$\min\left\{\sum_{i=1}\phi_{di} + \sum_{j=1}\phi_{Lj} + \sum_{p=1}\phi_{0p}\right\}$$
$$\text{subject to } \tau_g = 0. \qquad (2)$$

In this expression,

$$\phi_{di} = [\mathbf{d}_i - \mathbf{f}_i(\mathbf{m}_l)]^T[\mathbf{C}_{di}]^{-1}[\mathbf{d}_i - \mathbf{f}_i(\mathbf{m}_l)] \qquad (3)$$

is the sum of the normalized misfits of the ith group of data, which sense only the parameters of the lth model through the non-linear function $\mathbf{f}_i(\mathbf{m}_l)$. The data errors are assumed uncorrelated and represented by the covariance matrix $\mathbf{C}_{di}$. Similarly,

$$\phi_{Lj} = \alpha_j^2[\mathbf{Dm}_j]^T[\mathbf{Dm}_j] \qquad (4)$$

corresponds to the sum of the squares of the Laplacian values in the jth model weighted by the damping factor α_j^2 selected for each individual image.

$$\phi_{0p} = [\mathbf{m}_p - \mathbf{m}_{0p}]^T[\mathbf{C}_{0p}]^{-1}[\mathbf{m}_p - \mathbf{m}_{0p}] \qquad (5)$$

is the sum of the square of the closeness of the pth model to an a priori model $\mathbf{m}_{0p}$, normalized by the covariance matrix of the a priori model $\mathbf{C}_{0p}$.

[7] This objective function involves non-linear equations and is solved in an iterative scheme where the group of predicted observations is redefined, using Taylor series expansion, as

$$\mathbf{f}_i(\mathbf{m}_r^k) \cong \mathbf{f}_i(\mathbf{m}_r^{k-1}) + \mathbf{A}_{ir}^{k-1}(\mathbf{m}_r^k - \mathbf{m}_r^{k-1}), \qquad (6)$$

where k denotes the actual iterate and $\mathbf{A}_{ir}^{k-1}$ comprises the partial derivatives of the ith group of observables with respect to the rth group of model parameters, i.e. the corresponding Jacobian matrix. Similarly, the Taylor series

expansion of the generalized cross-gradient constraint when $|\nabla m_g^k| \neq 0$ leads to its linearized version:

$$\nabla m_g^k \times \nabla m_i^k \cong -\nabla m_g^{k-1} \times \nabla m_i^{k-1} + \sum_{j=1}^{n}\left[\left(-\delta_{g,j}\nabla m_i^{k-1}\right.\right.$$
$$\left.\left. + \delta_{i,j}\nabla m_g^{k-1}\right) \times \nabla m_j^k\right] = 0 \qquad (7)$$
$$\text{where } \delta_{i,j} = \begin{cases} 1 \text{ for } i = j \\ 0 \text{ otherwise.} \end{cases}$$

This group of constraints will be written as

$$\mathbf{B}^{k-1}\mathbf{m}^k = \mathbf{b}^{k-1}. \qquad (8)$$

where a row of $\mathbf{B}^{k-1}$ is a discrete scheme for the operator $(-\delta_{g,j}\nabla m_i^{k-1} + \delta_{i,j}\nabla m_g^{k-1}) \times \nabla$ applied to the set of n images embedded in the vector $\mathbf{m}^k$ at every position and the corresponding element of the vector $\mathbf{b}^{k-1}$ is given by $\nabla m_g^{k-1} \times \nabla m_i^{k-1}$.

[8] To produce the results shown below the pivot g-image is varied through iterations and subsurface positions, selecting the image with the largest gradient magnitude. This because, according to (2), a large parameter gradient can only result from the corresponding data and constitutes a remarkable structural feature that is less likely to fail on condition (1). Note that varying g also reduces the dominance of the structure of an individual image.

[9] When the linearized expressions (6) and (8) are introduced in the objective function (2), it is reduced to a least squares problem with linear equality constraints, which is solved using the Lagrange multiplier method [see *Gallardo and Meju*, 2004] to obtain

$$\mathbf{m}^k = \mathbf{m}_{LS}^{k-1} - \mathbf{C}_{LS}^{k-1}(\mathbf{B}^{k-1})^T\left(\mathbf{B}^{k-1}\mathbf{C}_{LS}^{k-1}(\mathbf{B}^{k-1})^T\right)^{-1}$$
$$\cdot\left[\mathbf{B}^{k-1}\mathbf{m}_{LS}^{k-1} + \mathbf{b}^{k-1}\right] \qquad (9)$$

where

$$\mathbf{m}_{LSi}^{k-1} = \mathbf{C}_{LSi}^{k-1}\sum_j\left\{\left(\mathbf{A}_{ji}^{k-1}\right)^T\mathbf{C}_{dj}^{-1}\left(\mathbf{d}_j - \mathbf{A}_{ji}^{k-1}\mathbf{m}_i^{k-1}\right)\right\} + \mathbf{C}_{00i}^{-1}\mathbf{m}_{0i} \qquad (10)$$

and $\left(\mathbf{C}_{LSi}^{k-1}\right)^{-1} = \sum_j\left\{\left(\mathbf{A}_{ji}^{k-1}\right)^T\mathbf{C}_{dj}^{-1}\mathbf{A}_{ji}^{k-1}\right\} + \alpha_i\mathbf{D}^T\mathbf{D} + \mathbf{C}_{00i}^{-1}.$
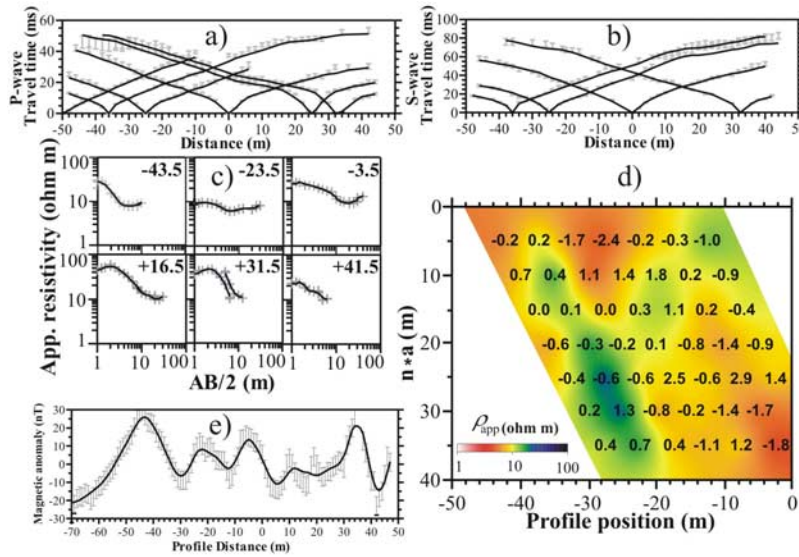
$$(11)$$

Figure 2. Geophysical data collected in Pumitas field site. (a) P- and (b) SH-wave travel times recorded for the first arrivals of two seismic refraction experiments. The grey bars correspond to the picking error estimates used to weight the inversion procedures, which varied from .1 to 3 ms in both cases. (c) VES data for the studied site (grey crosses), the annotated number indicates the center of the array. (d) Dipole-dipole electrical data (colored image) with annotated values of the normalized residuals based on a constant 5% estimated standard deviation for the data errors. (e) Magnetic data recorded in the studied site. The indicated grey bars are set to 5 nT as a good estimate of the magnetic data errors. In all the plots, the solid lines are the geophysical responses of their corresponding property models after multiple joint inversion.

Note that $\mathbf{m}_{LSi}$ corresponds to the conventional least squares estimates of the ith model with covariance $\mathbf{C}_{LSi}$. In (10) and (11) the jth index stands for any data type sensitive to the same ith group of model parameters. Thus, any parameter-coupled data such as those measured by magnetotelluric and DC surveys or seismic first and later arrivals can be simultaneously incorporated. For this application, cross-property type correlation apart from the structural constraint implicit in **B** was not included, thus $\mathbf{C}_{LS}$ is block diagonal having elements of the type (11), which allows the individual and independent computation of least-squares models ($\mathbf{m}_{LSi}$) and facilitates its computational manipulation. All these independent models are integrally corrected to make them geometrically similar according to (9). At every iteration, only the linearized cross-gradient constraint (7) is exactly satisfied, but it will lead to the non-linear cross-gradient constraint (1) when the process achieves full convergence.

[10] To test the program functionality and to demonstrate that the generalized cross-gradient constraint can lead to structurally similar images in actual geological terrains the algorithm was applied to multiple geophysical data from a field site as described next.

3. Joint Inversion of Field Data and Geospectral Imaging

[11] Pumitas field site is located in Ensenada, Mexico, over a metamorphosed volcaniclastic sequence of andesitic composition, which is partially covered by clastic deposits that filled the paleotopography. The area was prepared and leveled to host two football grounds and, therefore, there are no local topographical irregularities and only few shallow man-made disturbances. Several geophysical methods were deployed along an East-West trending, 100 m long, profile. This included two seismic deployments that yielded the P- and S-wave first arrivals presented in Figures 2a and 2b. The profiles included several shot points with vertical and lateral-ditch hammering, with geophones located every two-meters. The profile was also surveyed with 6 vertical electrical soundings (VES) and dipole-dipole profiling whose data are shown in Figures 2c and 2d, which were incorporated in the process of inversion for resistivity estimation. 121 total magnetic field data (shown in Figure 2e) were also measured. The magnetic inclination for the area is 56 degrees and the data were corrected for diurnal variations using a fixed reference magnetometer. The magnetic data did not show a marked regional trend thus a mean value was subtracted to reduce the search to local magnetization contrasts. All the data error estimates are indicated in the corresponding figures. These data constrain four subsurface parameters: v_P, v_S, electrical resistivity and magnetization. Data are related to model parameters by the algorithms of *Vidale* [1988] and *Hole and Zelt* [1995] for the P- and S-wave travel times, *Perez-Flores et al.* [2001] for the DC resistivity data and *Bhattacharyya* [1964] for the magnetic data. Whereas the Jacobian matrices required by (6) for DC resistivity and magnetic data are implicit in the adopted linear forward modeling solutions, the Jacobian matrix of the seismic data is computed by independent ray tracing.

[12] In a first experiment, the data were individually inverted, without cross-gradient constraint, maintaining equal damping factors ($\alpha = 1$), starting from a medium with P- and S-wave velocity that increases with depth and homogeneous resistivity and magnetization. The individual processes achieved a satisfactory convergence of 4% in less than 5 iterations. The four images so obtained achieved
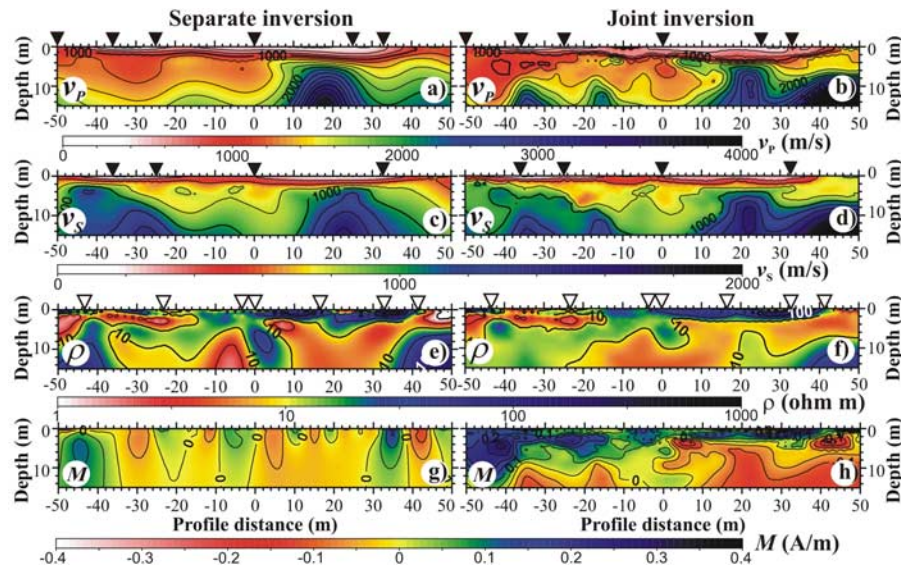
Figure 3. Multiple parameter images obtained for Pumitas field site. (a), (c), (e) and (g) images were obtained using conventional separate inversion while corresponding images (b), (d), (f) and (h) were obtained with the multiple cross-gradient joint inversion of the four geophysical data sets shown in Figure 2. Note the common structural control evinced for all the images after joint inversion.

satisfactory data fits ($\mathrm{rms}_{vp} = 1.50$, $\mathrm{rms}_{vs} = 1.25$, $\mathrm{rms}_{DC} = 0.95$ and $\mathrm{rms}_M = 0.37$) and produced the subsurface structures according to their own sensitivity as illustrated in Figure 3. It is noticeable that whereas the v_P, v_S and electrical images suggest a consistent structural control, the magnetic image depicts an incompatible structure.

[13] The field data were all simultaneously inverted using the algorithm developed for multiple cross-gradient joint inversion. The process involved the same regularization factors and initial model as the previous experiment and converged to a 4% level after 5 cycles. The images obtained are shown in Figures 3b, 3d, 3f and 3h, from which it can be seen that the four images depict a common underlying structure (as measured by the cross-gradient values listed in Table 1) that should be strongly representative of the local geology. The images found adequately fit their corresponding geophysical data as illustrated in Figure 2, achieving misfits 25 % larger than those of separate inversion ($\mathrm{rms}_{vp} = 1.78$, $\mathrm{rms}_{vs} = 1.52$, $\mathrm{rms}_{DC} = 1.22$ and $\mathrm{rms}_M = 0.72$). It is apparent that the increased geometrical resemblance of the individual images should facilitate their geological interpretation. Let us now proceed to show the advantages that a common structural framework brings into

the multiple cross-property analysis. For this purpose, I plotted a geospectral image using the v_P, resistivity and magnetization images in the form of a Red-Green-Blue (RGB) color image and superimposed the largest gradient areas of the v_S image, the fourth element in the geospectral image, as further indication of subsurface structure. The images obtained by separate inversion are merged in Figure 4a and those of joint inversion in Figure 4b. Note that the geospectral image obtained from the separate inversions highlights the structural differences of the individual models whereas the image obtained from the joint inversion neatly defines some characteristic zones of approximately homogeneous parameter values. For instance, Zone I delimitates a high velocity, low resistivity
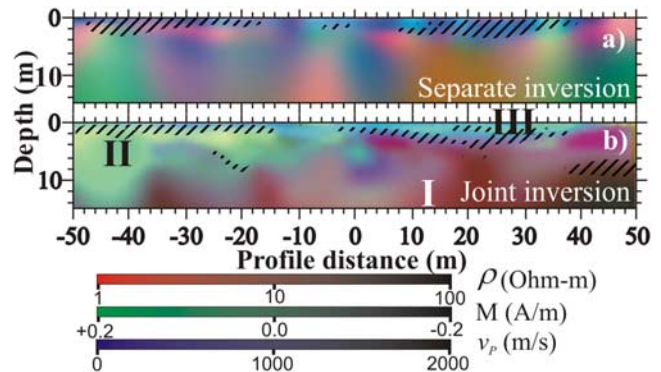

Figure 4. Geospectral image of resistivity (red), magnetization (green), and v_P (blue) parameters for Pumitas field site. The hatched areas indicate places with the largest v_S contrasts. (a) Image composed from the separately estimated images. (b) Image composed from the jointly inverted images. Note the salient subsurface structure and potential lithotype zones, enhanced on Figure 4b by the underlying common structural framework.

Table 1. RMS Values of the Corresponding Cross-Gradient Functions for Separately and Jointly (Values in Parentheses) Estimated Images

X	∇s_P,[a] $\times 10^{-3}$ s/m^2	∇s_S,[a] $\times 10^{-3}$ s/m^2	$\nabla \rho$, log(ohm m)/m	∇M, A/m^2
∇s_P[a]	0.0	(0.0028)	(0.0034)	(0.0008)
∇s_S[a]	0.0519	0.0	(0.0031)	(0.0008)
$\nabla \rho$	0.0829	0.1961	0.0	(0.0009)
∇M	0.0091	0.0230	0.0231	0.0

[a]Note that slowness is the inverted seismic parameter.

and low magnetization material that matches the underlying bedrock. Zone II shows different geophysical values that correlate to the clastic deposits over the eroded flank of bedrock material. Zone III could be explained by the overlying man-made ground.

[14] I envisage that the combined analysis of the constituent parameter values in the geospectral image will be of immense value for the search for multiple parameter cross-correlations that can help in lithology classification and the understanding of complex subsurface processes.

4. Conclusions

[15] A generalized cross-gradient constraint is proposed in this paper for finding geometrically concordant images from multiple subsurface data as a different geophysically plausible method of reducing the non-uniqueness inherent in inversion. The results show that it is possible to produce geometrically similar images with little penalty to the misfit function. The resulting geospectral image provides a natural visualization of the multiple subsurface parameters found and suggests that the joint inversion models are outlining characteristic geological units known to lie beneath, with reasonable parameter values. The results thus show that models with a common structural framework are a valuable analysis and interpretation tool.

References

Bhattacharyya, B. K. (1964), Magnetic anomalies due to prism-shaped bodies with arbitrary polarization, *Geophysics*, *29*, 517–531.

Gallardo, L. A., and M. A. Meju (2003), Characterization of heterogeneous near-surface materials by joint 2D inversion of dc resistivity and seismic data, *Geophys. Res. Lett.*, *30*(13), 1658, doi:10.1029/2003GL017370.

Gallardo, L. A., and M. A. Meju (2004), Joint two-dimensional DC resistivity and seismic travel time inversion with cross-gradients constraints, *J. Geophys. Res.*, *109*, B03311, doi:10.1029/2003JB002716.

Gallardo, L. A., and M. A. Meju (2007), Joint 2D cross-gradient imaging of magnetotelluric and seismic travel-time data for structural and lithological classification, *Geophys. J. Int.*, *169*, 1261–1272, doi:10.1111/j.1365-246X.2007.03366.x.

Gallardo, L. A., M. A. Meju, and M. A. Perez-Flores (2005), A quadratic programming approach for joint image reconstruction: mathematical and geophysical examples, *Inverse Problems*, *21*, 435–452.

Haber, E., and D. Oldenburg (1997), Joint inversion: A structural approach, *Inverse Problems*, *13*, 63–77.

Hole, J. A., and B. C. Zelt (1995), 3-D finite-difference reflection travel-times, *Geophys. J. Int.*, *121*, 427–434.

Linde, N., A. Binley, A. Tryggvason, L. B. Pedersen, and A. Revil (2006), Improved hydrogeophysical characterization using joint inversion of cross-hole electrical resistance and ground-penetrating radar traveltime data, *Water Resour. Res.*, *42*, W12404, doi:10.1029/2006WR005131.

Perez-Flores, M. A., S. Mendez-Delgado, and E. Gomez-Trevino (2001), Imaging low-frequency and dc electromagnetic fields using a simple linear approximation, *Geophysics*, *66*, 1067–1081.

Saunders, J. H., J. V. Herwanger, C. C. Pain, M. H. Worthington, and C. R. E. de Oliveira (2005), Constrained resistivity inversion using seismic data, *Geophys. J. Int.*, *160*, 785–796.

Tryggvason, A., and N. Linde (2006), Local earthquake (LE) tomography with joint inversion for P- and S-wave velocities using structural constraints, *Geophys. Res. Lett.*, *33*, L07303, doi:10.1029/2005GL025485.

Vidale, J. (1988), Finite-difference calculation of travel-times, *Bull. Seismol. Soc. Am.*, *78*, 2062–2076.

Zhang, J., and F. D. Morgan (1996), Joint seismic and electrical tomography, paper presented at EEGS Symposium on Applications of Geophysics to Engineering and Environmental Problems, Environ. and Eng. Geophys. Soc., Keystone, Colo.

————————————

L. A. Gallardo, Earth Science Division, CICESE, km 107 carretera Tijuana-Ensenada, Ensenada, Baja CA 22860, Mexico. (lgallard@cicese.mx)